Droop Control of Three- and Four-Leg Hybrid Parallel Inverters Based on Three-Phase Generalized Coordinate Transformation

Guangjun Tan, Yixing Zheng, Wei Zhao, Lei Qi, and Xiaofeng Sun, *Member, IEEE*

***Abstract*—In recent years, widespread adoption of three-leg inverters has been observed. However, there is often a need for three-phase four-wire inverters to provide a neutral connection for asymmetrical loads within microgrid contexts. This article proposes a three- and four-leg hybrid inverter parallel structure to address the above issues. The aim is to fulfill the four-wire requirement under asymmetrical load conditions and mitigate the voltage unbalance problem. The article begins by investigating the output voltage balance control of three- and four-leg inverters and the control techniques of the hybrid parallel system. Deficiencies in traditional power droop control and virtual impedance control under unbalanced conditions are identified by calculating the inverter's output power under asymmetric load conditions. To address these issues, the article adopts average power droop and proposes a novel virtual impedance method. This method considers the impact of line impedance differences on the distribution accuracy of active power and unbalanced load current, effectively improving their distribution accuracy. Connecting three- and four-leg inverters in parallel, the four-leg inverter is capable of significantly reducing the zero-sequence voltage of the common load terminal and enhances three-phase voltage balance. Finally, experimental results validate the feasibility and effectiveness of the improved virtual impedance control.**

***Index Terms*—Asymmetric loads, droop control, three- and four-leg inverters hybrid parallel, three-phase generalized coordinate transformation, virtual impedance.**

NOMENCLATURE

$U_1 \angle \delta_1, U_2 \angle \delta_2$	Output voltage phasor of the two inverters.
$E \angle 0^\circ$	Voltage phasor of the PCC point.
Z_{o1}, Z_{o2}	Output impedance of the two inverters.
Z_{l1}, Z_{l2}	Connecting line impedance of the two inverters.
P_1, P_2	Active power delivered to the load by the inverter.
Q_1, Q_2	Reactive power delivered to the load by the inverter.
$Z_i = R_i + X_i$	Total equivalent impedance of the inverter.
$R_i = R_{oi} + R_{li}$	Total equivalent resistance of the inverter.
$X_i = X_{oi} + X_{li}$	Connecting line reactance of the two inverters.
ω_n	Rated angular frequency.
ω_{com}	PCC point angular frequency.
U_n	Rated voltage.
P_n, Q_n	Rated active and reactive power.
K_P, K_Q	Voltage and frequency droop coefficient.
Z_{vir}, R_{vir}	Virtual resistance and impedance value.
p, q	Instantaneous active and reactive power output from the inverter.
$U_{droop1} \angle \delta_1$, $U_{droop2} \angle \delta_2$	Output voltage and phase of the two inverters obtained by droop control.
u_C	Capacitor voltages.
i_o	Inverter output currents.
i_{load}	Load currents.
$G(s)$	Inverter output transfer function.
$Z_o(s)$	Inverter output impedance transfer function.
$\varphi_{ba}, \varphi_{ca}$	Phase difference between b-phase and c-phase voltages exceeding the a-phase voltage.
k_{ba}, k_{ca}	Ratio of b-phase voltage and c-phase voltage respectively to the amplitude of a-phase voltage.
$C_\gamma(s)$	PI controller for phase-locked loops.
$\hat{\boldsymbol{\gamma}}_{u_C}$	Phase or amplitude-phase information of the capacitor voltages obtained from the PLL or APLL.
$\boldsymbol{\gamma}^*$	Reference amplitude and phase information.
$\boldsymbol{\gamma}_{i_L}$	Amplitude and phase information of the inductor currents.
p_{abc}	Outputs of the inner current control loop.
$\overline{P}, \overline{Q}$	Average average active and reactive power.
$\boldsymbol{U}_C^*$	Reference voltage obtained through capacitor voltages.
$\boldsymbol{U}^*$	Reference voltage obtained through droop control.
S_{nn}	Rated total capacity of the nth inverter.

Manuscript received 12 January 2024; revised 9 April 2024 and 22 June 2024; accepted 11 August 2024. Date of publication 16 August 2024; date of current version 7 October 2024. This work was supported in part by the Natural Science Foundation of China under Grant 61903320, in part by the Natural Science Foundation of Hebei Province under Grant E2021203162, and in part by the Key Research and Development Program of Hebei Province under Grant 19214405D. Recommended for publication by Associate Editor H. L. Ginn. *(Corresponding author: Xiaofeng Sun.)*

The authors are with the Key Lab of Power Electronics for Energy Conservation and Motor Drive of Hebei Province (Yanshan University), School of Electrical Engineering, Yanshan University, Qinhuangdao 066004, China (e-mail: 18333503128@126.com; 1327431838@qq.com; zwysu@ysu.edu.cn; qil@ysu.edu.cn; sxf@ysu.edu.cn).

Color versions of one or more figures in this article are available at https://doi.org/10.1109/TPEL.2024.3443882.

Digital Object Identifier 10.1109/TPEL.2024.3443882

$i_{oa1}, i_{ob1}, i_{oc1}$ Three-phase load current of the four-leg inverter after subtracting the zero-sequence load current.

$i_{oa2}, i_{ob2}, i_{oc2}$ Three-leg inverter three-phase load current.

I. Introduction

THE growing global energy and climate crises have propelled the rapid development of microgrids powered by renewable energy sources. As microgrid systems expand and loads increase, a single inverter's capacity becomes insufficient, necessitating parallel configuration with multiple inverters [1]. To ensure stability, it is imperative that coordinate output voltage amplitude and phase among parallel inverters. In addition, safe and reliable operation requires proportional distribution of total load power between inverters to minimize circulating currents and enhance system redundancy [2].

Currently, commonly used inverter parallel control methods can be categorized into two types: control with interconnecting line and control without interconnecting line. While the control method with interconnecting line exhibits superior equalization capability [3], [4], [5], [6], it comes with several disadvantages associated with the communication lines among inverters, leading to reduced flexibility, reliability, and system stability [7].

On the contrary, the interconnection line-free control method operates without the constraints of communication lines. Each inverter is independently controlled, enabling objectives such as plug-and-play and peer-to-peer control objectives. This approach enhances the redundancy and reliability of the microgrid system. The interconnection line-free control method is primarily based on droop control and has been widely adopted in recent years for the parallel control of inverters [8].

In high-voltage power grids, line impedance is usually inductive, and conventional active power-frequency P-f and reactive power-voltage Q-V droop control methods are typically applied [9]. However, in low-voltage microgrids, the line impedance tends to be resistive, and traditional droop control can amplify power coupling, thereby reducing system control performance. Literature [10] suggests using reactive power-frequency Q-f and active power-voltage P-V droop control to address power distribution control under resistive line impedance. For power coupling issues, the inverter impedance design method studied in literature [11], [12] achieves a proportional distribution of power but ignores the line impedance mismatch. Alternatively, researchers have proposed methods such as virtual V/f transformation [13] and virtual impedance control [14], [15] to realize power decoupling control.

The virtual impedance control method is widely adopted due to the challenges associated with the coordinate transformation method, which requires accurate line impedance information that is unpredictable and difficult to detect. However, these conventional enhancement approaches are typically designed for three-phase balanced systems [16], [17]. In three-phase unbalanced systems, it becomes essential to address the equalization of negative-sequence and zero-sequence load currents. For the issue of unbalanced load current distribution, interconnection-free line control methods, primarily involving droop control and virtual impedance control, are commonly employed.

Effectively parallel connecting two or more inverters should adhere to two fundamental principles: first, maintaining no circulating currents between inverters in steady state; second, ensuring as accurate as possible load current distribution despite potential line impedance mismatch [18].

The mismatch in line impedance under unbalanced loads leads to uneven inverter current distribution. This issue is addressed by injecting negative- and zero-sequence components into the inverter voltage through negative- and zero-sequence virtual impedance control. Essentially, this is equivalent to connecting a virtual impedance in series in front of the line impedance [19], [20].

As the four-leg inverter has higher control degree of freedom and each phase can be controlled independently, literature [21] constructs three-phase independent P-f/Q-V droop control and achieves unbalanced load current distribution through three secondary control actions, which ensures an equal division of power per phase and total power of the three phases, and at the same time achieves PCC voltage control. Literature [22], [23] extracts the balanced and unbalanced components of voltage and current based on the conservative power theory and adaptively calculates the magnitude of the unbalanced virtual impedance using a consensus-based distributed control scheme, which aims to share the unbalanced currents based on the residual capacity of each inverter, while regulating its degree of unbalance of output voltage to meet the IEEE power quality standards. Literature [24] and [25] analyzed the positive-, negative- and zero-sequence circuit model of the inverter parallel system and obtained that the negative- and zero-sequence components of the load currents are related to the total equivalent output impedance of the inverter, and the positive-sequence power droop control is used to realize the allocation of the positive-sequence load currents, and the accuracy of the allocation of the unbalanced load currents can be improved by the negative-sequence and zero-sequence virtual impedance control. Literature [26] injected ac small signals into the voltage feedthrough and achieved adaptive virtual impedance control through harmonics and unbalanced power droop aligned with the frequency of the injected ac small signals. However, the output voltage quality and system response speed are poor in this scheme.

Since three-phase load asymmetry leads to a negative sequence component in the output voltage, automatic compensation of the unbalanced voltage can be realized by the relationship between the negative sequence reactive power and the negative sequence voltage [27], [28]. However, the existing control scheme for unbalanced load current distribution is typically based on the symmetric component analysis method in the positive-negative-sequence dual synchronous coordinate system. The scheme involves numerous control loops and a complex control system, requiring the extraction of phase sequences for both voltage and current. For this reason, this article proposes the balanced control of inverter output voltage under asymmetrical load conditions and the load current equalization

control scheme for inverter parallel system based on a new type of three-phase generalized coordinate transformation.

In this article, unbalanced conditions are primarily addressed through a scheme of three-phase generalized coordinate transformation. These transformations include the Tan-Sun coordinate transformation [29] and the 3-D coordinate transformation [30]. The Tan-Sun coordinate transformation is applied in three-phase three-wire systems, while the 3-D coordinate transformation is used in three-phase four-wire systems. The control scheme based on three-phase generalized coordinate transformation has been compared with conventional positive-, negative-, and zero-sequence (PNZS) synchronous reference coordinate frames (SRFs) control strategy and resonant-based control methods [31]. Using the three-phase generalized coordinate transformation, the three-phase unbalanced signals can be directly decoupled into two or three dc signals. Thus, the tracking error can be fully compensated in the dq or dq0 coordinate system using the PI control method. In addition, this scheme reduces the number of controllers, simplifies the control structure, and addresses the problems of complex control structures, low transient response speed, and low stability margin found in traditional schemes.

The article is structured as follows. Section II overviews the inverter hybrid parallel system, droop control, and virtual impedance and analyzes the power control under unbalanced conditions. Section III details the average power droop control, and based on this, the virtual impedance control is implemented using the virtual impedance principle combined with the voltage balancing control strategy based on three-phase generalized coordinate transformation. Experimental results are presented in Section IV, respectively. Finally, Section V concludes the article.

II. Inverter Parallel System Power Control

A. The Hybrid Parallel System of Three- and Four-Leg Inverters

The hybrid parallel system of three-leg and four-leg inverters is shown in Fig. 1.

The hybrid parallel system consists of a three-leg and a four-leg inverter in parallel, where the three-leg inverter is controlled by using Tan-Sun coordinate transformation and the four-leg inverter is controlled by using 3-D coordinate transformation.

The transformation matrices of Tan-Sun coordinate transformation and the 3-D coordinate transformation is shown in (1) and (2), shown at the bottom of this page, and the inverse matrices

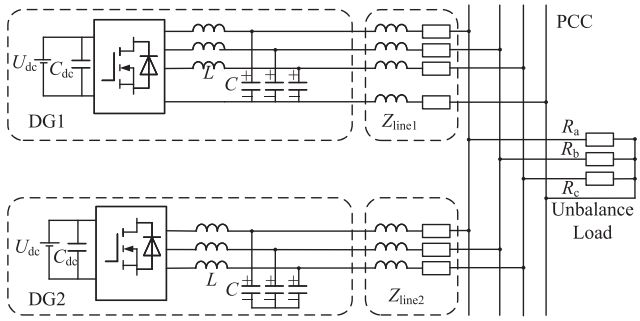

Fig. 1. Hybrid parallel system of three- and four-leg inverters.

of Tan-Sun coordinate transformation and the 3-D coordinate transformation is shown in the following:

$$\boldsymbol{T}_{\mathrm{Tan-Sun}}^{-1}=\begin{bmatrix}\frac{2}{\sqrt{3}}\sin(\varphi_{\mathrm{ba}}-\varphi_{\mathrm{ca}}) & 0 & 1\\ \frac{2}{\sqrt{3}}\cos\varphi_{\mathrm{ba}}\sin\varphi_{\mathrm{ca}} & -\frac{2}{\sqrt{3}}\sin\varphi_{\mathrm{ba}}\sin\varphi_{\mathrm{ca}} & 1\\ -\frac{2}{\sqrt{3}}\sin\varphi_{\mathrm{ba}}\cos\varphi_{\mathrm{ca}} & \frac{2}{\sqrt{3}}\sin\varphi_{\mathrm{ba}}\sin\varphi_{\mathrm{ca}} & 1\end{bmatrix} \tag{3}$$

and

$$M_{\mathrm{Tan-Sun}}=\sqrt{3}\left[\sin 2(\varphi_{ca}-\varphi_{ba})+\sin 2\varphi_{ba}-\sin 2\varphi_{ca}\right]$$

and (4), shown at the bottom of the next page.

The corresponding phase-locked loop (PLL) and amplitude-phase-locked loop (APLL) are required in the three-phase generalized coordinate transformation to obtain the amplitude and phase information φ_{ba}, φ_{ca}, k_{ab}, and k_{ac} of the capacitor voltages. The column vector form of the unbalance indicator for the Tan-Sun coordinate transformation can be expressed as $\boldsymbol{\gamma}_{u_C-1}=\begin{bmatrix}\varphi_{\mathrm{ba}} & \varphi_{\mathrm{ca}}\end{bmatrix}^{\mathrm{T}}$, and the column vector form of the unbalance indicator for the 3-D coordinate transformation can be expressed as $\boldsymbol{\gamma}_{u_C-2}=\begin{bmatrix}\varphi_{\mathrm{ba}} & \varphi_{\mathrm{ca}} & k_{\mathrm{ab}} & k_{\mathrm{ac}}\end{bmatrix}^{\mathrm{T}}$. If the three-phase signals are balanced, then

$$\boldsymbol{\gamma}_{u_C-1}=\begin{bmatrix}-\frac{2\pi}{3} & \frac{2\pi}{3}\end{bmatrix}^{\mathrm{T}}\triangleq\boldsymbol{\gamma}^*$$

$$\boldsymbol{\gamma}_{u_C-2}=\begin{bmatrix}-\frac{2\pi}{3} & \frac{2\pi}{3} & 1 & 1\end{bmatrix}^{\mathrm{T}}\triangleq\boldsymbol{\gamma}^*.$$

Balanced control of three-phase capacitor voltages can be realized by adjusting the unbalance indicator $\boldsymbol{\gamma}_{u_C}$. In the three-wire system, only the balanced control of three-phase positive-sequence capacitor voltages can be realized, while in

$$\boldsymbol{T}_{\mathrm{Tan-Sun}}=\frac{3}{M_{\mathrm{Tan-Sun}}}\begin{bmatrix}\cos(\varphi_{\mathrm{ba}}+\varphi_{\mathrm{ca}}) & \cos(\varphi_{\mathrm{ca}}-\varphi_{\mathrm{ba}}) & \cos(\varphi_{\mathrm{ba}}-\varphi_{\mathrm{ca}})\\ -\sin(\varphi_{\mathrm{ba}}+\varphi_{\mathrm{ca}}) & -\sin(\varphi_{\mathrm{ca}}-\varphi_{\mathrm{ba}}) & -\sin(\varphi_{\mathrm{ba}}-\varphi_{\mathrm{ca}})\\ \frac{1}{3} & \frac{1}{3} & \frac{1}{3}\end{bmatrix} \tag{1}$$

$$\boldsymbol{T}_{\mathrm{3D}}=\frac{1}{M_{\mathrm{3D}}}\begin{bmatrix}2\sin 2\left(\varphi_{\mathrm{ca}}-\varphi_{\mathrm{ba}}\right) & -2k_{\mathrm{ab}}\sin 2\varphi_{\mathrm{ca}}\cos\varphi_{\mathrm{ba}} & 2k_{\mathrm{ac}}\sin 2\varphi_{\mathrm{ba}}\cos\varphi_{\mathrm{ca}}\\ 0 & 2k_{\mathrm{ab}}\sin 2\varphi_{\mathrm{ca}}\sin\varphi_{\mathrm{ba}} & -2k_{\mathrm{ac}}\sin 2\varphi_{\mathrm{ba}}\sin\varphi_{\mathrm{ca}}\\ \sin\left(\varphi_{\mathrm{ba}}-\varphi_{\mathrm{ca}}\right) & k_{\mathrm{ab}}\sin\varphi_{\mathrm{ca}} & -k_{\mathrm{ac}}\sin\varphi_{\mathrm{ba}}\end{bmatrix}. \tag{2}$$

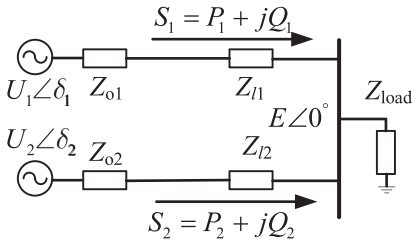

Fig. 2. Single-phase equivalent circuit diagram of inverter parallel system.

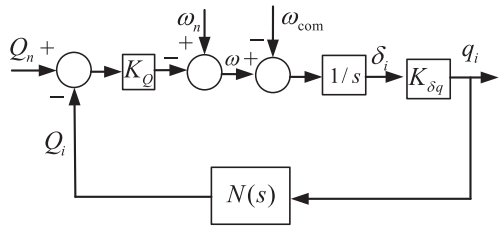

Fig. 3. Closed-loop block diagram of Q-f droop control.

the four-wire system, the amplitude and phase balanced control of three-phase capacitor voltages can be realized independently.

The specific design process of the PLL and APLL for the three-phase generalized coordinate transformation is described in detail in [29] and [30].

B. Droop Control

In an islanded microgrid system, due to the lack of voltage and frequency support from the larger grid, it is necessary to control the output voltage amplitude and frequency of each inverter to synchronize the operation among inverters to ensure the stable operation of the whole system. The simplified single-phase equivalent circuit diagram of the inverter-parallel system is presented in Fig. 2.

Based on the circuit principle, it can be deduced that the active and reactive power delivered by the inverter to the load are

$$P_i = \frac{E\left(R_i\left(U_i\cos\delta_i - E\right) + U_i X_i \sin\delta_i\right)}{R_i^2 + X_i^2} \tag{5a}$$

$$Q_i = \frac{E\left(X_i\left(U_i\cos\delta_i - E\right) - U_i R_i \sin\delta_i\right)}{R_i^2 + X_i^2}. \tag{5b}$$

In this article, we mainly consider the low-voltage microgrid where the line impedance is mainly resistive [32] which can be expressed as $Z_i \approx R_i$ and the phase difference is usually small, which can be seen as $\cos\delta_i \approx 1$ and $\sin\delta_i \approx \delta_i$, ignoring the influence of the inductive component of the line impedance, (5) can be simplified as

$$P_i = \frac{E(U_i - E)}{R_i} \tag{6a}$$

$$Q_i = \frac{-U_i E\delta_i}{R_i}. \tag{6b}$$

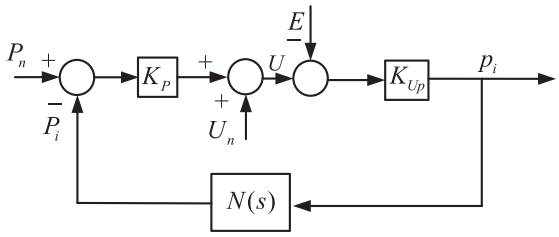

Fig. 4. Closed-loop block diagram of P-V droop control.

From (6), there exists an approximate positive linear correlation between the inverter output active power and the difference between the inverter output voltage and the voltage at the PCC point. Simultaneously, there is an approximate negative linear correlation between the inverter output reactive power and the phase difference δ. Therefore, adjusting δ indirectly by altering the frequency achieves the regulation of reactive power, while the active power is distributed by adjusting the inverter output voltage U. The P-f/Q-V droop control equation adopted based on this relationship is as follows [33] :

$$\omega_i = \omega_n - K_Q(Q_n - Q_i) \tag{7a}$$

$$U_i = U_n + K_P(P_n - P_i). \tag{7b}$$

According to (6) and (7), the closed-loop block diagram of Q-f/P-V droop control can be obtained as shown in Figs. 3 and 4, respectively:

Literature [34] derives the active power p_i and reactive power q_i expressions in the frequency domain based on the closed-loop control block diagram, and calculates the active power and reactive power expressions at steady state based on the final value theorem. By analyzing the steady-state active power p_i and reactive power q_i expressions, it is concluded that in Q-f droop control, adjusting the droop coefficients can realize the

$$\boldsymbol{T}_{3D}^{-1} = \begin{bmatrix} 1 & 0 & 4\cos\varphi_{ba}\cos\varphi_{ca} \\ \dfrac{1}{k_{ab}}\cos\varphi_{ba} & -\dfrac{1}{k_{ab}}\sin\varphi_{ba} & \dfrac{4}{k_{ab}}\cos\varphi_{ba}\cos\left(\varphi_{ca}-\varphi_{ba}\right) \\ \dfrac{1}{k_{ac}}\cos\varphi_{ca} & -\dfrac{1}{k_{ac}}\sin\varphi_{ca} & \dfrac{4}{k_{ac}}\cos\varphi_{ca}\cos\left(\varphi_{ca}-\varphi_{ba}\right) \end{bmatrix} \tag{4}$$

and

$$M_{3D} = \sin 2(\varphi_{ca} - \varphi_{ba}) + \sin 2\varphi_{ba} - \sin 2\varphi_{ca}.$$

equal or proportional distribution of reactive power, while in P-V droop control, the existence of voltage drop caused by the difference of the line impedance results in the impossibility of realizing the distribution of the active power by adjusting the droop coefficients alone. When inverters of the same capacity are connected in parallel, as long as the droop coefficients are equal and the total output impedance of the inverters are equal, the active power can be equally divided; when inverters of different capacities are connected in parallel, it is guaranteed that the ratio of the total output impedance of the inverters and the droop coefficients are inversely proportional to the ratio of the inverters rated capacity, so as to realize the proportionate distribution of active power according to the rated capacity.

C. Analysis of Power Control Under Unbalanced Operating Conditions

It is evident from the analysis in Section II-B that Q-f/P-V droop control can achieve active and reactive power distribution among inverters under balanced conditions, ensuring the stable operation of the system. However, in the presence of asymmetrical three-phase loads, the output power components of the inverters change, posing some challenges if traditional Q-f/P-V droop control is still employed [35]. Under conditions of load asymmetry, to maintain balanced output capacitor voltages, the load current must be unbalanced. Using the symmetrical component method, the expression for the load current can be formulated as

$$i_{\mathrm{oa}} = I^{+}\cos(\omega t+\theta^{+}) + I^{-}\cos(\omega t+\theta^{-}) + I^{0}\cos(\omega t+\theta^{0}) \tag{8a}$$

$$i_{\mathrm{ob}} = I^{+}\cos(\omega t+\theta^{+}-2\pi/3) + I^{-}\cos(\omega t+\theta^{-}+2\pi/3) + I^{0}\cos(\omega t+\theta^{0}) \tag{8b}$$

$$i_{\mathrm{oc}} = I^{+}\cos(\omega t+\theta^{+}+2\pi/3) + I^{-}\cos(\omega t+\theta^{-}-2\pi/3) + I^{0}\cos(\omega t+\theta^{0}). \tag{8c}$$

The output capacitor voltages are mainly a positive sequence component, ignoring the negative and zero sequence components

$$U_{C\mathrm{a}} = U\cos\omega t \tag{9a}$$

$$U_{C\mathrm{b}} = U\cos(\omega t-2\pi/3) \tag{9b}$$

$$U_{C\mathrm{c}} = U\cos(\omega t+2\pi/3). \tag{9c}$$

Instantaneous apparent power

$$\left\{ s = p+jq = \tfrac{3}{2}u_{\alpha\beta}\bar{i}_{\alpha\beta}. \right. \tag{10}$$

The instantaneous active power and instantaneous reactive power output from the inverter can be calculated:

$$p = P + p_{c2} = 1.5UI^{+}\cos\theta^{+} + 1.5UI^{-}\cos(2\omega t+\theta^{-}) \tag{11a}$$

$$q = Q + p_{s2} = -1.5UI^{+}\sin\theta^{+} + 1.5UI^{-}\sin(2\omega t+\theta^{-}). \tag{11b}$$

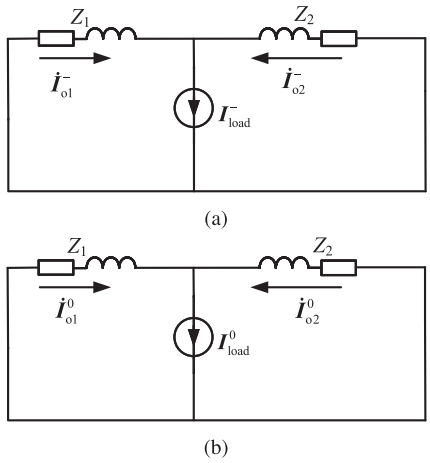

Fig. 5. Inverter parallel equivalent circuit diagram. (a) Negative Sequence. (b) Zero sequence.

From (11), when the load is asymmetrical, both instantaneous active power and instantaneous reactive power contain dc components and second harmonic components.

In unbalanced working conditions, the introduction of the negative sequence power second harmonic component into the droop equation induces fluctuations in the control system, impacting the system's stability. Traditional positive sequence power droop or average power droop control functions to droop the dc portion of the instantaneous power, achieving positive sequence load current distribution. However, under asymmetrical load conditions, it is necessary to distribute both negative sequence load current and zero sequence load current through appropriate control.

For ease of analysis, the negative sequence voltage and zero sequence voltage are assumed to be 0 when the control objective is balanced. The symmetrical component method can then be applied to obtain the negative sequence and zero sequence equivalent circuit diagrams of the inverter parallel under unbalanced conditions, as illustrated in Fig. 5. In the figure, Z_i represents the total equivalent output impedance of the inverter, i.e., the sum of line impedance and control equivalent output impedance. At this time, the distribution of negative sequence and zero sequence load currents depends on the connection line impedance between inverters and the equivalent output impedance of the controller.

From Fig. 5, the negative and zero sequence currents of each inverter are as follows:

$$i^{-}_{\mathrm{ol}} = \frac{Z_2}{Z_1+Z_2}i^{-}_{\mathrm{load}} \tag{12a}$$

$$i^{0}_{\mathrm{o1}} = \frac{Z_2}{Z_1+Z_2}i^{0}_{\mathrm{load}}\,. \tag{12b}$$

From (12), the negative-sequence and zero-sequence load currents of each inverter are influenced by the total equivalent output impedance of the inverter. Therefore, control of negative-sequence and zero-sequence current distribution can be achieved by manipulating the negative-sequence and zero-sequence equivalent output impedance of the inverter.

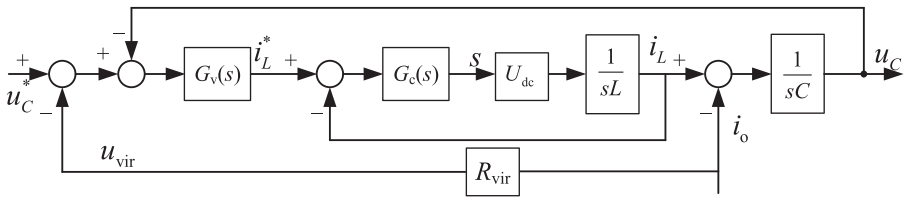

Fig. 6. Block diagram of voltage-current closed-loop control with addition of virtual impedance.

D. Virtual Impedance

Analyzing in Section II-B, the frequency-related reactive power can automatically be distributed in accordance with the droop coefficients of the Q-f droop curves. However, voltage-related active power is influenced by the line impedance parameter, and variations in line impedance result in decreased accuracy in active power allocation. To achieve load power equalization and load current equalization among inverters, virtual impedance control is commonly employed [36].

The schematic diagram of the virtual impedance implementation is shown in Fig. 6.

According to Fig. 6 and the analytical method of reference [34], the transfer function of the inverter output voltage can be obtained as

$$\begin{aligned} u_C(s) &= G(s)u_C^*(s) - i_o(s)Z_o(s) \\ &= \frac{G_v(s)G_c(s)U_{dc}}{s^2LC + sCG_c(s)U_{dc} + G_v(s)G_c(s)U_{dc}}u_C^*(s) \\ &= -\frac{G_v(s)G_c(s)U_{dc}R_{vir} + (sL + G_c(s)U_{dc})}{s^2LC + sCG_c(s)U_{dc} + G_v(s)G_c(s)U_{dc}}i_o(s) \end{aligned} \tag{13}$$

where the parameters of $G_v(s)$ and $G_c(s)$ are obtained according to [30].

Substituting the circuit parameters into (13) yields the Bode plots of $G(s)$ and $Z_o(s)$ as depicted in Fig. 7. In Fig. 7(a), it is observed that, when the system is controlled in $dq0$ coordinate system, the voltage-current signals are transformed into constant dc signals. The amplitude of $G(s)$ in the low-frequency band within 0–10 Hz is 1, and the phase angle is 0°, enabling zero steady-state error control of the voltage. Fig. 7(b) illustrates that the low-frequency band $Z_o(s)$ within 0–10 Hz is inductive and has a small impedance value before the addition of virtual impedance. After adding the virtual resistance, the output impedance of the inverter $Z_o(s)$ becomes resistive, with the impedance value approximately equal to the virtual resistance value.

The aforementioned virtual impedance control can regulate the inverter output voltage as $\boldsymbol{u}_c = \boldsymbol{u}_c^* - \boldsymbol{i}_o R_{vir}$, which is equivalent to connecting a virtual resistor R_{vir} in series before the line impedance. By adjusting the size of the virtual resistor R_{vir}, the total output impedance characteristics of the inverter can be modified. The parallel equivalent circuit diagram of the inverter after adding the virtual impedance is illustrated in Fig. 8.

In the low-voltage microgrid system, the impedance ratio r/X of the line impedance is approximately 7.7, with the resistive

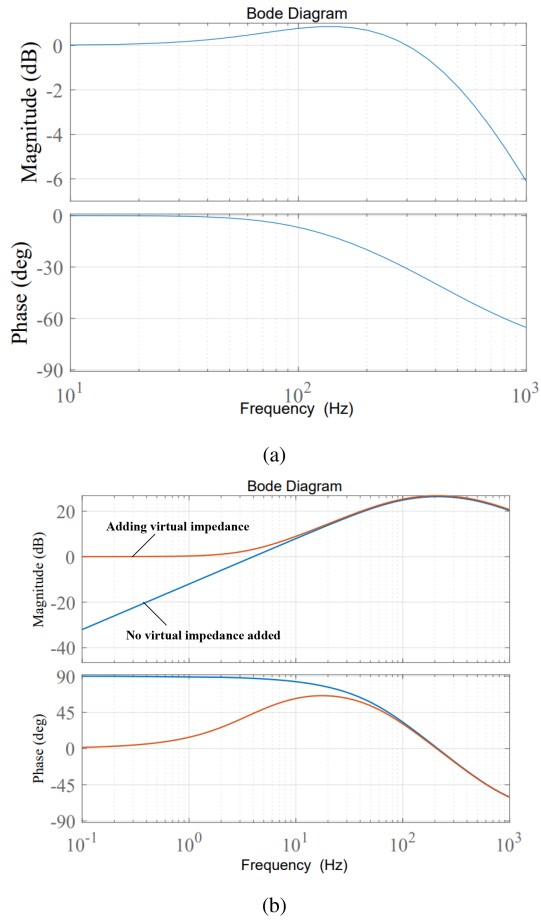

Fig. 7. Bode diagram of closed-loop system. (a) $G(s)$. (b) $Z_o(s)$.

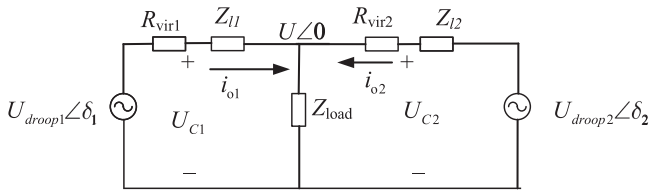

Fig. 8. Inverter parallel equivalent circuit diagram after adding virtual impedance control.

value in the line impedance playing a dominant role. By adjusting the value of the virtual resistor such that $R_{vir} \gg R_{l1}$, make the total equivalent output impedance of the inverter primarily influenced by virtual impedance. This reduction is the impact of the line impedance parameter the precision of power distribution. Furthermore, adding the virtual resistor increases

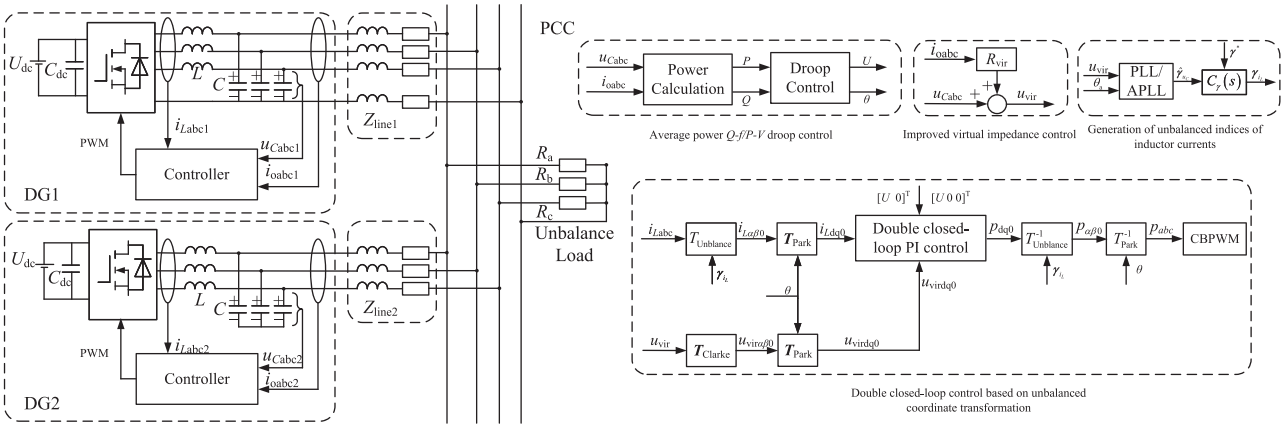

Fig. 9. Three- and four-leg inverter control block diagram.

the system's damping capacity, enhancing the overall system stability.

III. Unbalanced Load Current Distribution Based on Virtual Impedance

In the presence of three-phase load asymmetry, the zero-sequence component of the load current is solely born by the four-leg inverter. Therefore, the three and four-leg inverters in the hybrid inverter parallel system should share both the positive-sequence component and the negative-sequence component of the load current. As discussed in Section II, positive-sequence load current can be distributed and controlled from the perspective of power distribution. Meanwhile, the negative-sequence load current can be adjusted through virtual impedance control to achieve distribution control by modifying the total equivalent output impedance of the inverter. In addition, positive-sequence virtual impedance control can enhance the accuracy of average power allocation.

Given that the positive and negative sequence equivalent circuits of the parallel inverters are identical, uniform positive and negative sequence virtual impedance control can be realized in the abc coordinate system. Balancing control of the inverter output voltage is also necessary. The block diagrams depicting the parallel control of three- and four-leg inverters based on droop control under unbalanced conditions are presented in Fig. 9.

The left side of Fig. 9 shows the parallel topology of the two inverters and the right side presents the structure of the controller. The control structure is delineated into four main components: the first part involves average power Q-f/P-V droop control, the second part employs virtual impedance control, the third part includes the generation of unbalanced indices of inductor currents for the PLL for Tan-Sun coordinate transformation in a three-leg inverter or the APLL for 3-D coordinate transformation in a four-leg inverter, and the fourth part includes the voltage-current inner loop control for handling unbalanced loads. $\boldsymbol{T}_{\text{unbalance}}$ corresponds to $\boldsymbol{T}_{\text{Tan-Sun}}$ in a three-leg inverter and $\boldsymbol{T}_{\text{3D}}$ in a four-leg inverter, and $\boldsymbol{T}^{-1}_{\text{unbalance}}$ corresponds to $\boldsymbol{T}^{-1}_{\text{Tan-Sun}}$ in a three-leg inverter and $\boldsymbol{T}^{-1}_{\text{3D}}$ in a four-leg inverter, respectively.

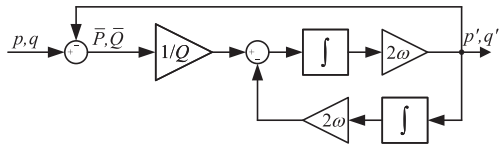

Fig. 10. Average power calculation.

Literature [30] comprehensively describes the 3-D coordinate transformation applied to four-leg inverters and also provides voltage, current loop design schemes, while three-leg inverters [29] have similarities with four-leg inverters.

A. Average Power Droop Control

From (11), it is evident that under unbalanced conditions, second harmonic power pulsations manifest in the instantaneous active power and reactive power of the inverter output. If the instantaneous power is directly introduced into the droop control equations, it will result in second harmonic pulsations appearing in the inverter voltage and frequency references. This, in turn, affects the performance and stability of the entire control system. To mitigate this issue, a low-pass filter is typically employed to filter out the second harmonic pulsations in the instantaneous power p, q. However, the use of a low-pass filter impacts the dynamic response speed of the entire control system. In this article, the trap method based on the second-order generalized integrator (SOGI) is employed to filter out the second harmonic frequency power pulsations and obtain the average power $\overline{P}$, $\overline{Q}$. The structure is depicted in Fig. 10.

In Fig. 10, Q represents the quality factor of the traps, and ω is the grid angular frequency obtained from the droop control.

Based on Fig. 10, the average active power and average reactive power can be determined. Combining these with the droop control equations shown in (7), the voltage and angular frequency reference of the inner loop can be obtained, and the angle θ is the integral of the angular frequency:

$$\theta = \int (\omega_n - K_Q(Q_n - Q_i))dt \tag{14a}$$

$$U_i = U_n + K_P(P_n - P_i) \tag{14b}$$

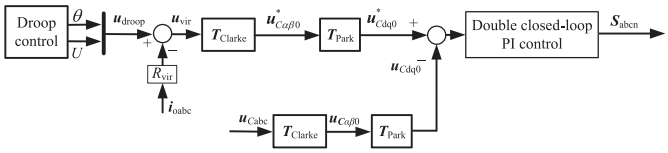

Fig. 11. Control block diagram of virtual impedance realization with $\boldsymbol{u}_C$ as the control target.

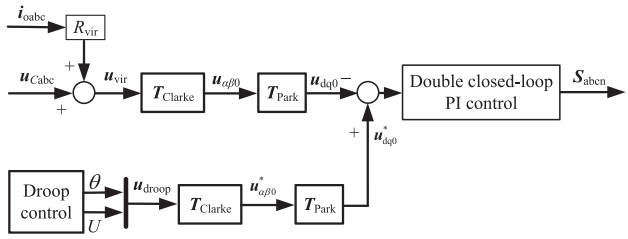

Fig. 12. Control block diagram of virtual impedance realization with $\boldsymbol{u}_C + \boldsymbol{i}_o R_{vir}$ whole as control target.

where $\omega_n = 100\,\pi$ rad/s, $U_n = 311$, and K_P and K_Q can be selected according to the permissible voltage and frequency deviations, as well as requirements for rapid response.

The U_i obtained from the average power Q-f/P-V droop control is utilized as the voltage of the inner voltage loop reference, i.e., $\boldsymbol{U}_C^* = [U_i\ 0]^{\mathrm{T}}$ or $\boldsymbol{U}_C^* = [U_i\ 0\ 0]^{\mathrm{T}}$. The angle θ is applied in the coordinate transformation.

B. Virtual Impedance Under Three-Phase Generalized Coordinate Transformation

From Section II-C, it is evident that the negative-sequence and zero-sequence currents between inverters primarily depend on the total output equivalent impedance of the inverter, therefore, the equivalent output impedance of inverters can be changed by injecting the negative-sequence voltage component $\boldsymbol{u}_C^- = \boldsymbol{i}_o^- Z_{vir}$ and the zero-sequence voltage component $\boldsymbol{u}_C^0 = \boldsymbol{i}_o^0 Z_{vir}$ into the output voltage of the inverter. To achieve this control objective, a voltage-current double closed-loop control is utilized to realize the steady-state error-free tracking of the negative-sequence and zero-sequence voltages.

The scheme of controlling the positive, negative, and zero-sequence components of the capacitor voltages based on the symmetric component method in the positive, negative, and zero-sequence dq coordinate system is widely used. However, in this control scheme, an additional control loop is introduced, increasing the complexity of the control system. In addition, there is a need to extract positive, negative, and zero-sequence components from the voltage and current. In order to avoid the extraction of positive and negative sequence components, this chapter performs virtual impedance control in the abc coordinate system.

In order to realize virtual impedance control, the three-phase capacity voltage of the inverter is generally used as the control target, so that it tracks $\boldsymbol{u}_C^* - \boldsymbol{i}_o R_{vir}$, where is the three-phase symmetrical voltage obtained by $\boldsymbol{u}_C^*$ droop control. Its control block diagram is shown in Fig. 11.

In practice, under unbalanced conditions, reducing the unbalance of the capacitor voltages is essential for enhancing the accuracy of load current distribution. However, if the inverter three-phase capacitor voltages is still used as the control objective and the Clarke and Park transformations are employed to obtain the $dq0$ or dq component, a second harmonic component will be present in the dq component. The PI controller cannot be realized on the ac signals to achieve zero-steady-state error compensation, which affects control performance.

By combining the voltage and current inner loop control scheme proposed in the literature [30], the traditional virtual impedance implementation method is refined. The entire

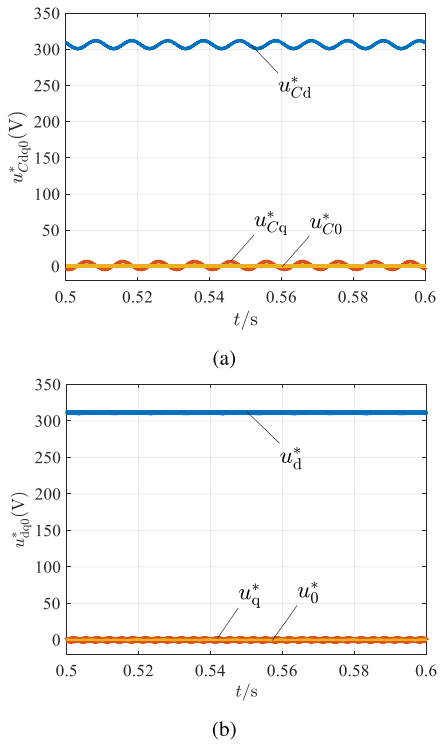

Fig. 13. Coordinate transformed reference voltage. (a) u^*_{Cdq0}. (b) u^*_{dq0}.

$\boldsymbol{u}_C + \boldsymbol{i}_o R_{vir}$ is considered as the control object, ensuring it tracks the three-phase symmetrical voltage $\boldsymbol{u}^*$ obtained from the droop control. At steady state, $\boldsymbol{u}_C + \boldsymbol{i}_o R_{vir} = \boldsymbol{u}^*$ achieves the same virtual impedance effect. In addition, $\boldsymbol{u}_C + \boldsymbol{i}_o R_{vir}$ as a whole represents a three-phase balanced alternating current signal. Employing Clarke and Park transformations to the $dq0$ or dq coordinate system yields a constant dc signal,enabling it to achieve zero-steady-state error in the final output of the capacitor voltages through PI control. Its control block diagram is shown in Fig. 12.

Comparing the two virtual impedance control methods and comparing the simulation Fig. 13, it can be found that using the conventional control method, the control target is $\boldsymbol{u}_C$, which is used as the reference voltage to be transformed to the dq0 coordinate system by Clarke and Park transformation, there are second harmonic components in its d-axis component $\boldsymbol{u}^*_{Cd}$ and q-axis component $\boldsymbol{u}^*_{Cq}$. This affects the control performance and results in the average active power and load current not being equalized, but using the proposed control scheme to change the control target to $\boldsymbol{u}_C + \boldsymbol{i}_o R_{vir}$, there are no second harmonic

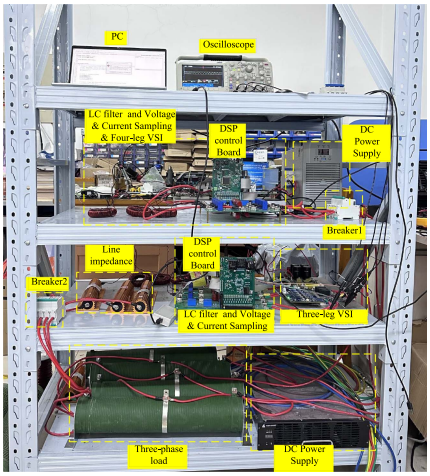

Fig. 14. Physical diagram of three- and four-leg inverter hybrid parallel experimental platform.

components of the d-axis component $\boldsymbol{u}_{\mathrm{q}}^{*}$ and the q-axis component $\boldsymbol{u}_{\mathrm{q}}^{*}$ in the reference voltage, which effectively improves the control effect.

To achieve the unbalanced load distribution requirement, the virtual resistor value can be set to

$$R_{\mathrm{vir1}}S_{\mathrm{n1}} = R_{\mathrm{vir2}}S_{\mathrm{n2}} = \cdots = R_{\mathrm{virn}}S_{nn} \tag{15}$$

To enhance load current distribution accuracy, the virtual resistance value should be set significantly higher than the line impedance value. However, an excessively large virtual resistance value can lead to increased voltage deviation and unbalance in the load voltage. The selection of the virtual resistance value should be based on the required voltage deviation and the desired degree of unbalance in the actual load voltage.

IV. Experimental Results

In order to verify the hybrid parallel control strategy of three- and four-leg inverters under asymmetric load conditions proposed in this paper, an experimental platform is built, and experimental verification is carried out as shown in the Fig. 14. The experimental parameters are listed in Table I. In this study, we primarily focus on the low-voltage microgrid, where the line impedance is predominantly resistive. In the experiment, the line impedance Z_{l1} of the four-leg inverter is set to $0.5\ \Omega$, and the line impedance Z_{l2} of the three-leg inverter is set to $1\ \Omega$. The hybrid parallel connection of two same-capacity three- and four-leg inverters is examined under both three-phase symmetric and asymmetric load conditions.

The three-phase symmetrical load is initially set to $R_{\mathrm{a}} = R_{\mathrm{b}} = R_{\mathrm{c}} = 20\ \Omega$. At a certain moment, a $30\ \Omega$ resistor is connected in parallel at both ends of the c-phase load, causing the three-phase load to transition from symmetrical to asymmetrical. The experimental waveforms obtained are shown below.

A. Power Calculation

Fig. 15 shows the instantaneous active power p, the average active power P, the instantaneous reactive power q, and the average reactive power Q of the inverter output under the load

TABLE I
Experimental Parameters

Symbol	Description	Value
U_{c}^{*}	Reference amplitude of ac voltage	311 V(50 Hz)
U_{dc}	DC bus voltage	700 V
L	LC filter inductance	2 mH
C	LC filter capacitance	14.1 μF
Z_{l1}	Line impedance 1	0.5 Ω
Z_{l2}	Line impedance 2	1 Ω
f_s	Switching frequency	10 kHz
Droop Control		
P_{n}	Rated active power	10 kW
Q_{n}	Rated reactive power	0.1 kvar
R_{vir}	Virtual resistance	0.5 Ω
K_P	P-V droop coefficient	0.00006
K_Q	Q-f droop coefficient	0.0006
Q	Trap quality factor	1
Current controllers $C_{\mathrm{c}}(s)$ (units have been ignored)		
k_{pc}	Proportional coefficient	12.566
k_{ic}	Integral coefficient	578.053
Voltage controllers $C_{\mathrm{v}}(s)$ (units have been ignored)		
k_{pv}	Proportional coefficient	0.048
k_{iv}	Integral coefficient	143.000
PLL		
ω_{c}	crossover frequency	50 πrad/s
Adjustment mechanism $C_{\gamma}(s)$ for γ_{i_L}		
$k_{\mathrm{p}\gamma}$	Proportional coefficient	1
$k_{\mathrm{i}\gamma}$	Integral coefficient	50 πrad/s

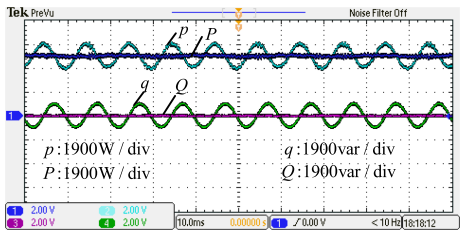

Fig. 15. Output power waveform of inverter.

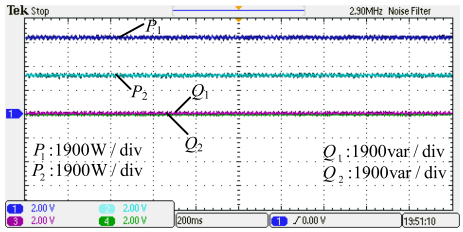

Fig. 16. Average power waveforms of the two inverter outputs without virtual impedance added.

asymmetry condition. It can be observed from the figure that, under the three-phase load asymmetry condition, the trapping method based on SOGI is used to filter out the second harmonic components in the instantaneous active power and reactive power. The obtained average active power and average reactive power only contain the dc component.

B. Average Power Droop Control

The average active and reactive power output from the two inverters is shown in Fig. 16.

In the Fig. 16, P_1 and Q_1 represent the average active power and average reactive power output from the four-leg inverter,

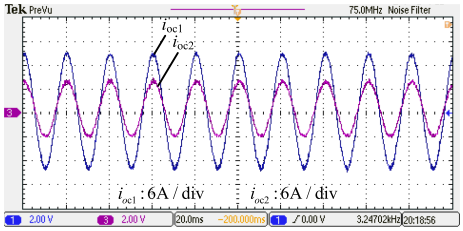

Fig. 17. Waveform of c-phase load current for two inverters without virtual impedance added.

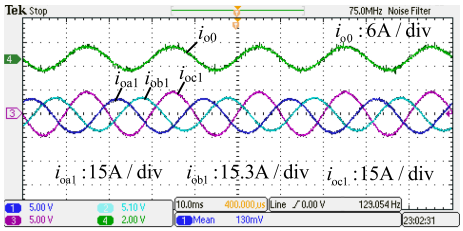

(a)

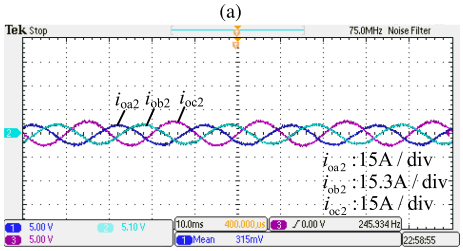

(b)

Fig. 18. Waveform of load current output from two inverters without virtual impedance added. (a) $\boldsymbol{i}_{\text{oabc1}}$-$i_{\text{o0}}$. (b) $\boldsymbol{i}_{\text{oabc2}}$.

while P_2 and Q_2 represent the average active power and average reactive power output from the three-leg inverter. From the figure, it is evident that with Q-f/P-V droop control, the average reactive power output from the two inverters can be evenly distributed. In the case of a purely resistive common load, the average reactive power output from both inverters is very small and close to 0var. However, due to the difference in line impedance, the average active power output from the two inverters follows a ratio of $P_1 : P_2 \approx 2 : 1 = Z_{l2} : Z_{l1}$.

The c-phase load currents of the two inverters are shown in Fig. 17.

Given that a zero-sequence current is present in the load current of the four-leg inverter under asymmetric loading conditions, while there is no zero-sequence current in the load current of the three-leg inverter, the zero-sequence load current circulates only in the four-leg inverter. Analyzing Fig. 17, it is apparent that i_{oc1} is approximately twice as large as i_{oc2}, roughly equal to the inverse of the inverter line impedance.

The three-phase load currents and zero-sequence currents of the two inverters are illustrated in Fig. 18. In the case of three-phase load asymmetry, as the zero-sequence current circulates only in the four-leg inverter, the three- and four-leg inverters are expected to collectively bear the three-phase unbalanced load currents after eliminating the zero-sequence load currents. However, as observed in Fig. 18, the three-phase load currents of

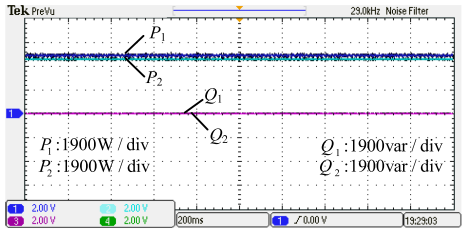

(a)

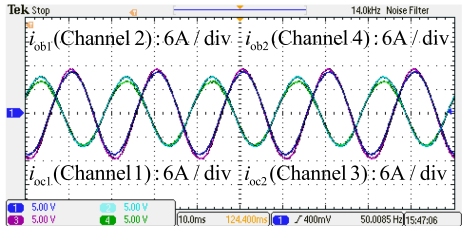

(b)

Fig. 19. Traditional virtual impedance scheme. (a) Average output power. (b) Output load currents.

the two inverters cannot be evenly distributed due to differences in line impedance.

The analysis of the experimental data indicates that the inverter-parallel system can operate stably when only Q-f/P-V droop control, combined with voltage-current inner-loop control, is employed. However, disparities in line impedance lead to uneven distribution of average active power and load current output from the inverters. In such scenarios, the ratio of average active power output and load current from the two inverters is approximately equal to the inverse of the line impedance of the inverters connected to the common load.

C. Virtual Impedance Control

To mitigate the impact of the difference in connection line impedance on the inverter output average power and three-phase load current distribution, a virtual resistor of $0.5\ \Omega$ is introduced to the control of the four-leg inverter. When the scheme with the control objective $\boldsymbol{u}_C$ is employed, after virtual impedance is added, the average output power and load current output waveforms of the two inverters in steady state are shown in Fig. 19.

From Fig. 19, it can be seen that when using the traditional control scheme with the control objective $\boldsymbol{u}_C$, there are errors in the distribution of the average active power and unbalanced load current output of the two inverters in steady state.

When the scheme with the control objective $\boldsymbol{u}_C + \boldsymbol{i}_{\text{o}} R_{\text{vir}}$ is employed, after virtual impedance is added, the average output power and load current output waveforms of the two inverters are shown in Fig. 20.

In Fig. 20, it is observed that after introducing virtual impedance, the average active power output from the two inverters becomes equalized around 100 ms. In a steady state, active power is equalized due to the addition of virtual impedance. The reactive power is only frequency dependent in the P-V/Q-f droop control. The reactive power is evenly distributed both before and after adding the virtual impedance.

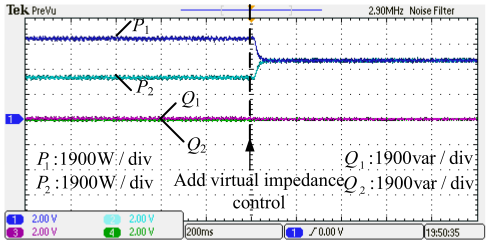

Fig. 20. Average output power waveforms of two inverters using improved virtual impedance scheme.

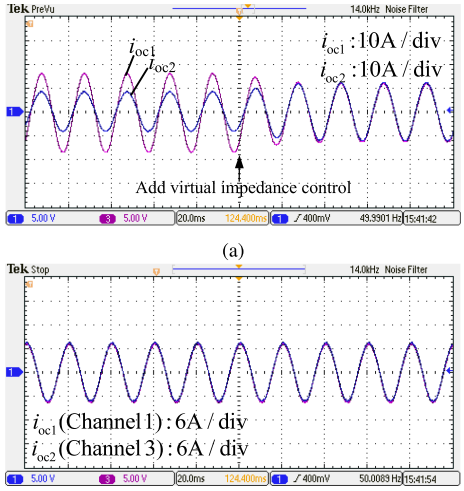

Fig. 21. Experimental waveforms of c-phase load current of two inverters using improved virtual impedance scheme. (a) Transient state. (b) Steady state.

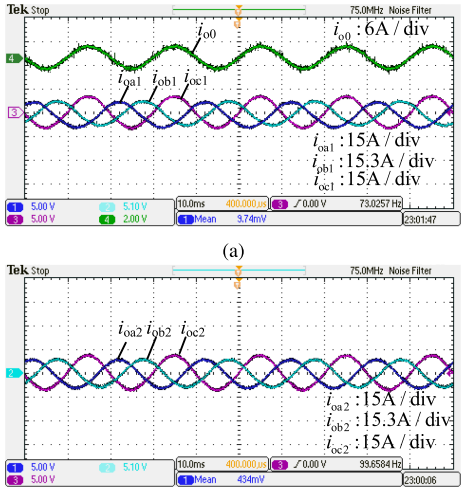

Fig. 22. Experimental waveforms of three-phase load current of two inverters using improved virtual impedance scheme. (a) $\boldsymbol{i}_{\mathrm{oabc1}}$-$i_{\mathrm{o0}}$. (b) $\boldsymbol{i}_{\mathrm{oabc2}}$.

The load current waveforms of the two inverters after adding the virtual impedance using the control scheme with the control objective of $\boldsymbol{u}_C + \boldsymbol{i}_{\mathrm{o}} R_{\mathrm{vir}}$ are shown in Figs. 21 and 22, respectively.

From Fig. 21(a), the addition of virtual impedance control current response time is about 40 ms.

TABLE II
COMPREHENSIVE COMPARISON

Accuracy error	Traditional control method	Improved control method
Active power distribution error	180 W	10 W
Load current distribution error	0.5 A	0.02 A

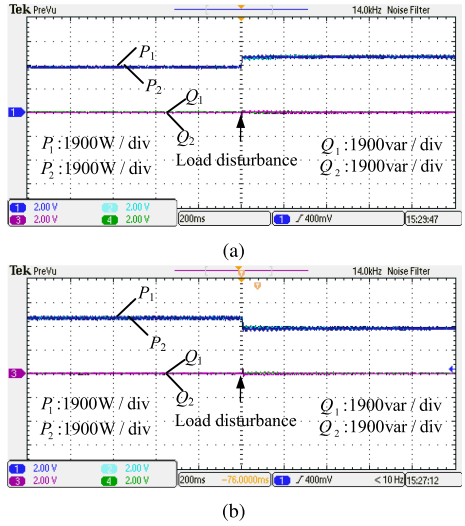

Fig. 23. Average power waveforms of the two inverter outputs during c-phase load disturbance. (a) Unbalanced load step on. (b) Unbalanced load step off.

Figs. 21 and 22 demonstrate that with the addition of virtual impedance control, the two inverters achieve an equal distribution of unbalanced load currents (positive-sequence and negative-sequence components) in the steady state, while the zero-sequence load currents are solely carried by the four-leg inverters.

By comparing the traditional control method in Fig. 11 with the improved control method proposed in Fig. 12 of this article, a comprehensive comparison is presented in Table II. The results show that the use of the improved control method can effectively reduce the distribution error of active power and load current.

When the c-phase is connected and disconnected with a 30 Ω resistor, the average power output and load current waveforms of the two inverters are as shown in Figs. 23 and 24.

From Figs. 23 and 24, it can be seen that when the load is switched, the average active power output from the two inverters is equalized around 200 ms, and the load current of the two inverters is equalized around 400 ms.

The three-phase capacitor voltages waveforms of the three- and four-leg inverter before and after adding the virtual impedance are illustrated in Figs. 25 and 26, respectively.

From Fig. 25, it can be observed that the three-phase capacitor voltages of the three-leg inverter remain balanced before and after adding the virtual impedance.

As shown in Fig. 26, the three-phase capacitor voltages of the four-leg inverter is balanced before adding virtual impedance. After adding virtual impedance, due to the unbalance in the

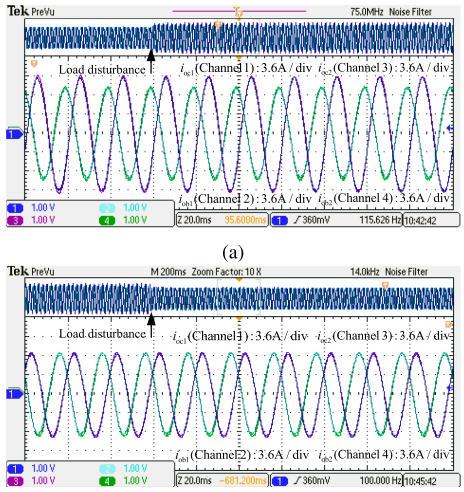

Fig. 24. Output load current waveforms of the two inverters during C-phase load disturbance. (a) Unbalanced load step on. (b) Unbalanced load step off.

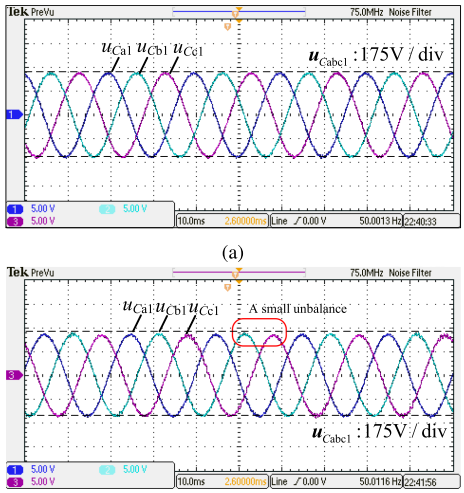

Fig. 26. Experimental waveforms of output voltages of four-leg inverter. (a) Before adding virtual impedance. (b) After adding virtual impedance.

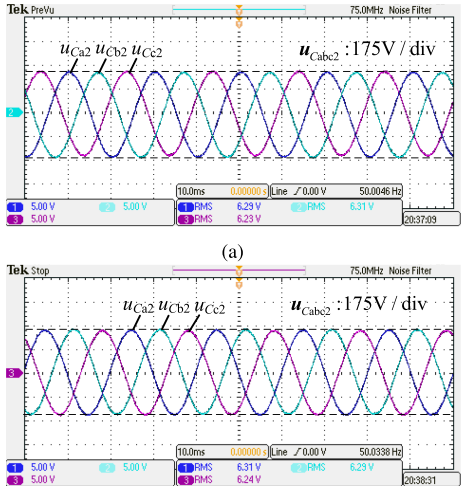

Fig. 25. Experimental waveforms of output voltage of three-leg inverter. (a) Before adding virtual impedance. (b) After adding virtual impedance.

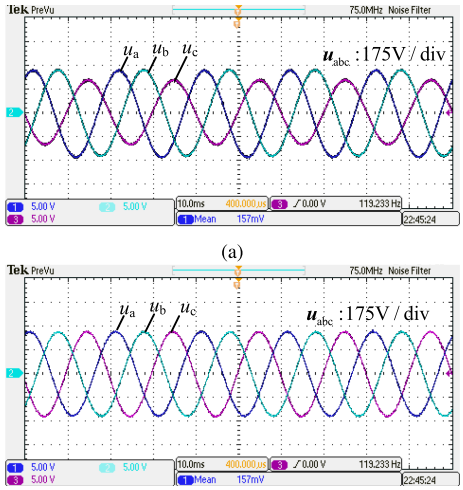

Fig. 27. Common load terminal voltages. (a) Single three-leg inverter. (b) Hybrid parallel connection of three- and four-leg inverters.

three-phase load current, virtual impedance control is implemented through load current feed-forward. At this point, the c-phase load current is larger compared to the other two-phase currents, resulting in a slightly smaller c-phase capacitor voltages than the other two-phase capacitor voltages. Consequently, there is a small unbalance in the three-phase capacitor voltages of the four-leg inverter.

D. Common Load Terminal Voltage

The voltage at the common load terminal when using a single three-leg inverter and a hybrid three- and four-leg inverter in parallel is shown in Fig. 27.

From Fig. 27(a), it can be observed that under asymmetrical load conditions, when a single three-leg inverter is used to supply power to three-phase loads, the structural limitations of the three-leg inverter prevent the control of the zero-sequence voltages. This results in a large zero-sequence voltage at the common load terminal, and the three-phase voltages unbalance fails to meet the load power supply demand. In contrast, Fig. 27(b) illustrates that by employing a three- and four-leg inverter hybrid parallel connection, the four-leg inverter can effectively control the zero-sequence voltage. This control mechanism significantly reduces the zero-sequence voltage at the common load terminal and enhances the balance of the three-phase voltages. Thus, the validity and feasibility of the hybrid parallel topology of three- and four-leg inverters are demonstrated.

V. Conclusion

In this article, a novel control strategy is introduced to address the limitations observed in traditional droop control and virtual impedance control when applied in unbalanced working conditions. The proposed strategy integrates virtual impedance control with voltage balancing control, employing a three-phase generalized coordinate transformation. By adjusting the control objective and combining the voltage balancing control strategy with the generalized coordinate transformation, a control effect

similar to traditional virtual impedance control is achieved. The entire control system is then transformed into the dq or $dq0$ coordinate system through PI control, facilitating steady-state error-free tracking of the dc signal. Experiments validate the effectiveness of the proposed three- and four-leg hybrid parallel control scheme. The strategy successfully manages the zero-sequence voltage, reduces the zero-sequence component of the voltage at the common load terminal, and improves voltage balance. The average power Q-f/P-V droop control ensures fair distribution of average power output from each inverter, while virtual impedance control alleviates the impact of line impedance differences on the accuracy of average active power and unbalanced load current distribution. This approach achieves precise equalization of load power and unbalanced load current for each inverter.

REFERENCES

[1] B. Kroposki, C. Pink, R. DeBlasio, H. Thomas, M. Simoes, and P. K. Sen, "Benefits of power electronic interfaces for distributed energy systems," *IEEE Trans. Energy Convers.*, vol. 25, no. 3, pp. 901–908, Sep. 2010.

[2] J. J. Justo, F. Mwasilu, J. Lee, and J.-W. Jung, "Ac-microgrids versus dc-microgrids with distributed energy resources: A review," *Renewable Sustain. Energy Rev.*, vol. 24, pp. 387–405, 2013.

[3] M. E. Kamalesh, M. Vikashini, and S. Pradeep, "Precompensated master slave control of parallel DC-DC converter in dc-microgrid," in *Proc. Int. Conf. Curr. Trends Towards Converging Technol.*, 2018, pp. 1–5.

[4] A. A. Eajal et al., "Stochastic centralized dispatch scheme for AC/DC hybrid smart distribution systems," *IEEE Trans. Sustain. Energy*, vol. 7, no. 3, pp. 1046–1059, Jul. 2016.

[5] M. Castilla, A. Camacho, J. Miret, M. Velasco, and P. Martí, "Local secondary control for inverter-based islanded microgrids with accurate active power sharing under high-load conditions," *IEEE Trans. Ind. Electron.*, vol. 66, no. 4, pp. 2529–2539, Apr. 2019.

[6] T.-F. Wu, Y.-K. Chen, and Y.-H. Huang, "3C strategy for inverters in parallel operation achieving an equal current distribution," *IEEE Trans. Ind. Electron.*, vol. 47, no. 2, pp. 273–281, Apr. 2000.

[7] Y. Wei, C. Min, C. Jingjing, Z. Junpeng, and Q. Zhaoming, "An improved wireless control strategy for parallel operation of distributed generation inverters," *Trans. China Electrotechnical Soc.*, vol. 23, no. 1, pp. 84–89, 2008.

[8] C. Wang, Z. Yang, and Z. Wu, "Design and realization of practical photovoltaic microgrid," *Electric Power Automat. Equip.*, vol. 31, no. 6, pp. 6–10, 2011.

[9] X. Meng, J. Liu, and Z. Liu, "A generalized droop control for grid-supporting inverter based on comparison between traditional droop control and virtual synchronous generator control," *IEEE Trans. Power Electron.*, vol. 34, no. 6, pp. 5416–5438, Jun. 2019.

[10] M. Qianping and C. Ming, "P-V/Q-F droop control strategy with virtual impedance for low-voltage microgrid with multiple micro sources," *Power Syst. Protection Control*, vol. 46, no. 1, pp. 96–102, 2018.

[11] J. Guerrero, L. G. de Vicuna, J. Matas, M. Castilla, and J. Miret, "Output impedance design of parallel-connected UPS inverters with wireless load-sharing control," *IEEE Trans. Ind. Electron.*, vol. 52, no. 4, pp. 1126–1135, Aug. 2005.

[12] J. M. Guerrero, N. Berbel, J. Matas, L. G. de Vicuna, and J. Miret, "Decentralized control for parallel operation of distributed generation inverters in microgrids using resistive output impedance," in *Proc. IECON 2006-32nd Annu. Conf. IEEE Ind. Electron.*, 2006, pp. 5149–5154.

[13] Y. Li and Y. W. Li, "Virtual frequency-voltage frame control of inverter based low voltage microgrid," in *2009 IEEE Elect. Power Energy Conf.*, 2009, pp. 1–6.

[14] Q. Zhang, C. Peng, Y. Chen, G. Jin, and A. Luo, "A control strategy for parallel operation of multi-inverters in microgrid," in *Zhongguo Dianji Gongcheng Xuebao(Proceedings of the Chinese Society of Electrical Engineering)*, vol. 32, no. 25. Chinese Society for Electrical Engineering, 2012, pp. 126–132.

[15] A. S. Vijay, N. Parth, S. Doolla, and M. C. Chandorkar, "An adaptive virtual impedance control for improving power sharing among inverters in islanded AC microgrids," *IEEE Trans. Smart Grid*, vol. 12, no. 4, pp. 2991–3003, Jul. 2021.

[16] X. Sun, Y. Hao, Q. Wu, X. Guo, and B. Wang, "A multifunctional and wireless droop control for distributed energy storage units in islanded AC microgrid applications," *IEEE Trans. Power Electron.*, vol. 32, no. 1, pp. 736–751, Jan. 2017.

[17] H. Mahmood, D. Michaelson, and J. Jiang, "Accurate reactive power sharing in an islanded microgrid using adaptive virtual impedances," *IEEE Trans. Power Electron.*, vol. 30, no. 3, pp. 1605–1617, Mar. 2015.

[18] D. De and V. Ramanarayanan, "Decentralized parallel operation of inverters sharing unbalanced and nonlinear loads," *IEEE Trans. Power Electron.*, vol. 25, no. 12, pp. 3015–3025, Dec. 2010.

[19] J. He, Y. W. Li, and F. Blaabjerg, "An enhanced islanding microgrid reactive power, imbalance power, and harmonic power sharing scheme," *IEEE Trans. Power Electron.*, vol. 30, no. 6, pp. 3389–3401, Jun. 2015.

[20] C. Burgos-Mellado et al., "Single-phase consensus-based control for regulating voltage and sharing unbalanced currents in 3-wire isolated ac microgrids," *IEEE Access*, vol. 8, pp. 164882–164898, 2020.

[21] E. Espina, R. Cárdenas-Dobson, M. Espinoza-B., C. Burgos-Mellado, and D. Sáez, "Cooperative regulation of imbalances in three-phase four-wire microgrids using single-phase droop control and secondary control algorithms," *IEEE Trans. Power Electron.*, vol. 35, no. 2, pp. 1978–1992, Feb. 2020.

[22] C. Burgos-Mellado, R. Cárdenas, D. Sáez, A. Costabeber, and M. Sumner, "A control algorithm based on the conservative power theory for cooperative sharing of imbalances in four-wire systems," *IEEE Trans. Power Electron.*, vol. 34, no. 6, pp. 5325–5339, Jun. 2019.

[23] C. Burgos-Mellado et al., "Distributed control strategy based on a consensus algorithm and on the conservative power theory for imbalance and harmonic sharing in 4-wire microgrids," *IEEE Trans. Smart Grid*, vol. 11, no. 2, pp. 1604–1619, Mar. 2020.

[24] J. Chen, B. Zhao, X. Chen, M. Liu, and C. Gong, "Droop control of three-phase four-wire parallel inverters under unbalanced load condition," *Diangong Jishu Xuebao/transactions China Electrotechnical Soc.*, vol. 33, no. 20, pp. 4790–4801, 2018.

[25] X. Zhou, F. Tang, P. C. Loh, X. Jin, and W. Cao, "Four-leg converters with improved common current sharing and selective voltage-quality enhancement for islanded microgrids," *IEEE Trans. Power Del.*, vol. 31, no. 2, pp. 522–531, Apr. 2016.

[26] B. Liu, Z. Liu, J. Liu, R. An, H. Zheng, and Y. Shi, "An adaptive virtual impedance control scheme based on small-AC-signal injection for unbalanced and harmonic power sharing in islanded microgrids," *IEEE Trans. Power Electron.*, vol. 34, no. 12, pp. 12333–12355, Dec. 2019.

[27] M. Savaghebi, A. Jalilian, J. C. Vasquez, and J. M. Guerrero, "Autonomous voltage unbalance compensation in an islanded droop-controlled microgrid," *IEEE Trans. Ind. Electron.*, vol. 60, no. 4, pp. 1390–1402, Apr. 2013.

[28] P.-T. Cheng, C.-A. Chen, T.-L. Lee, and S.-Y. Kuo, "A cooperative imbalance compensation method for distributed-generation interface converters," *IEEE Trans. Ind. Appl.*, vol. 45, no. 2, pp. 805–815, Mar./Apr. 2009.

[29] G. Tan, J. Cheng, and X. Sun, "Tan-sun coordinate transformation system theory and applications for three-phase unbalanced power systems," *IEEE Trans. Power Electron.*, vol. 32, no. 9, pp. 7352–7380, Sep. 2017.

[30] G. Tan, J. Wei, W. Zhao, L. Qi, and X. Sun, "Application of three-dimensional unbalanced coordinate transformation to stand-alone four-leg voltage-source inverter," *IEEE Trans. Power Electron.*, vol. 37, no. 10, pp. 11686–11703, Oct. 2022.

[31] I. Vechiu, O. Curea, and H. Camblong, "Transient operation of a four-leg inverter for autonomous applications with unbalanced load," *IEEE Trans. Power Electron.*, vol. 25, no. 2, pp. 399–407, Feb. 2010.

[32] H. Laaksonen, P. Saari, and R. Komulainen, "Voltage and frequency control of inverter based weak LV network microgrid," in *Proc. Int. Conf. Future Power Syst.*, 2005, p. 6.

[33] A. El Moubarek Bouzid, P. Sicard, A. Yamane, and J.-N. Paquin, "Simulation of droop control strategy for parallel inverters in autonomous ac microgrids," in *Proc. 8th Int. Conf. Modelling, Identification Control*, 2016, pp. 701–706.

[34] R.-J. Wai, Q.-Q. Zhang, and Y. Wang, "A novel voltage stabilization and power sharing control method based on virtual complex impedance for an off-grid microgrid," *IEEE Trans. Power Electron.*, vol. 34, no. 2, pp. 1863–1880, Feb. 2019.

[35] X. Zhou, X. M. Jin, F. Tang, and Y. B. Tong, "Islanded-mode control and implementation of a three-phase four-leg based microgrid converter under unbalanced load conditions," *Power Syst. Protection Control*, vol. 41, no. 19, pp. 24–31, 2013.

[36] J. He, Y. W. Li, J. M. Guerrero, F. Blaabjerg, and J. C. Vasquez, "An islanding microgrid power sharing approach using enhanced virtual impedance control scheme," *IEEE Trans. Power Electron.*, vol. 28, no. 11, pp. 5272–5282, Nov. 2013.

Guangjun Tan was born in Heilongjiang, China, in 1984. He received the B.E., M.E., and D.E. degrees in electrical engineering from Harbin Institute of Technology, Harbin, China, in 2006, 2008, and 2014, respectively.

In 2013, he joined the School of Electrical Engineereing, Yanshan University, Qinhuangdao, China, as a Lecturer. Since 2019, he has been an Associate Professor. His current research interest include grid-connected inverter control, microgrid stability control, advanced coordinate transformation, and advanced phase-locked loop.

Yixing Zheng received the B.E. degree in electrical engineering in 2022, from Yanshan University, Qinhuangdao, China, where he is currently working toward the M.E. degree in electrical engineering.

His current research interests include microgrids and decentralized paralleling of inverters.

Wei Zhao received the B.S. and M.S. degrees in electrical engineering and power electronics and power drives and the Ph.D. degree in power electronics and power drives from Yanshan University, Qinhuangdao, China, in 2006, 2009, and 2020, respectively.

His current research interests include the stability analysis of microgrid, energy router, partial power conversion.

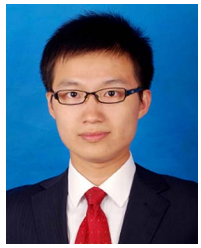

Lei Qi received the B.S. and M.S. degrees in electrical engineering and the Ph.D. degree in power electronics from Yanshan University, Qinhuangdao, China, in 2014, 2017, and 2023, respectively.

He was a Lecturer with Yanshan University, Qinhuangdao, China,. His current research interests include the energy management, nanogrids, and stability analysis.

Xiaofeng Sun (Member, IEEE) received the B.S. degree in electrical engineering from Northeast Heavy Machinery Institute, Heilongjiang, China, in 1993, and the M.S. and Ph.D. degrees in power electronics from Yanshan University, Qinhuangdao, China, in 1999 and 2005, respectively.

From 2003 to 2007, he was an Associate Professor with Yanshan University, where he has been a Professor since 2008. He is also the Director with the Key Laboratory of Power Electronics for Energy Conservation and Motor Drive of Hebei Province. He has authored or coauthored more than 70 transactions and conference papers. His research interests include dc–dc converters, multiple-input converters, hybrid electric vehicles, microgrids, and power quality control.